HHS Public Access

Author manuscript

Invest Radiol. Author manuscript; available in PMC 2023 November 01.

Published in final edited form as:

Invest Radiol. 2022 November 01; 57(11): 764–772. doi:10.1097/RLI.0000000000000885.

Extended intraoperative longitudinal 3D CBCT imaging with a continuous multi-turn reverse helical scan

Tess Reynolds, Ph. D[1], **Yiqun Q. Ma, BSc**[2], **Andrew J. Kanawati, M. D.**[3], **Alex Constantinidis, M. D.**[3], **Zoe Williams, B.Sc.**[1], **Grace Gang, Ph. D**[2], **Owen Dillon, Ph. D**[1], **Tom Russ, MSc**[4], **Wenying Wang, BEng**[2], **T. Ehtiati, Ph. D**[5], **Clifford. R. Weiss, M. D.**[2], **Nicholas Theodore, M. D.**[2], **Jeffery H. Siewerdsen, Ph. D**[2], **Joseph W. Stayman, Ph. D**[2], **Ricky T. O'Brien, Ph. D**[1]

[1]The University of Sydney, Sydney, Australia

[2]Johns Hopkins University, Baltimore, United States of America

[3]Westmead Hospital, Sydney, Australia

[4]University of Mannheim, Baden-Württemberg, Germany

[5]Siemens Healthcare, Baltimore, United States of America

Abstract

Objectives: Cone Beam Computed Tomography (CBCT) imaging is becoming an indispensable intraoperative tool; however, the current field-of-view prevents visualization of long anatomical sites, limiting clinical utility. Here, we demonstrate the longitudinal extension of the intraoperative CBCT field-of-view using a multi-turn reverse helical scan and assess potential clinical utility in interventional procedures.

Materials and Methods: A fixed-room robotic CBCT imaging system, with additional real-time control, was used to implement a multi-turn reverse helical scan. The scan consists of C-arm rotation, through a series of clockwise and anticlockwise rotations, combined with simultaneous programmed table translation. The motion properties and geometric accuracy of the multi-turn reverse helical imaging trajectory were examined using a simple geometric phantom. To assess potential clinical utility, a pedicle screw posterior fixation procedure in the thoracic spine from T1 to T12, was performed on an ovine cadaver. The multi-turn reverse helical scan was used to provide post-operative assessment of the screw insertion via cortical breach grading and mean screw angle error measurements (axial and sagittal) from 2 observers. For all screw angle measurements, the intraclass correlation coefficient (ICC) was calculated to determine observer reliability.

Results: The multi-turn reverse helical scans took 100 s to complete and increased the longitudinal coverage by 370% from 17 cm to 80 cm. Geometric accuracy was examined by comparing the measured to actual dimensions (0.2 ± 0.1 mm) and angles (0.2 ± 0.1 °) of a simple

Corresponding author contact: Telephone: +61 431419689, tess.reynolds@sydney.edu.au, Address: C81 Level 2, Room 207, Biomedical Building (The University of Sydney), 1 Central Ave, Eveleigh, NSW 2015, Australia.

Disclaimer: The concept and information presented in this paper is based on research and is not commercially available. Due to regulatory reasons, its future availability cannot be guaranteed.

geometric phantom, indicating that the multi-turn reverse helical scan provided sub millimeter and degree accuracy with no distortion. During the pedicle screw procedure in an ovine cadaver, the multi-turn reverse helical scan identified 4 cortical breaches, confirmed via the post-operative CT scan. Directly comparing the screw insertion angles ($n = 22$) measured in the post-operative multi-turn reverse helical and CT scans revealed an average difference of 3.3 ± 2.6° in axial angle and 1.9 ± 1.5° in the sagittal angle from 2 expert observers. The ICC was above 0.900 for all measurements (axial and sagittal) across all scan types (conventional CT, multi-turn reverse helical and conventional CBCT), indicating excellent reliability between observers.

Conclusions: Extended longitudinal field-of-view intraoperative 3D imaging with a multi-turn reverse helical scan is feasible on a clinical robotic CBCT imaging system, enabling long anatomical sites to be visualized in a single image, including in the presence of metal hardware.

Keywords

Cone-Beam CT; Interventional Imaging; Musculoskeletal

Introduction

Intraoperative 3D cone beam computed tomography (CBCT) imaging is increasingly being used during orthopedic surgeries, to improve hardware placement accuracy (1), to reduce surgical revision probability (2), and to shorten operative time (3). Intraoperative CBCT imaging is commonly provided by mobile O-arm and C-arm imaging systems, allowing easy integration with existing surgical room configurations (4–6). Drawing from the experiences of other disciplines, there has been a recent increase in the use of hybrid operating rooms with integrated fixed-room robotic CBCT imaging systems during orthopedic procedures (7). A key limitation of intraoperative CBCT imaging, whether using mobile or fixed-room systems, is the limited longitudinal coverage (i.e., along the length of the patient). While there is a growing body of work using mobile systems to implement long length intraoperative 2D imaging techniques (8, 9), it is currently not possible to capture the entire spine from sacral to cervical vertebrae or aorta (abdominal and thoracic), for example, in a single CBCT image intraoperatively. Focusing on musculoskeletal interventions, such imaging limitations have hindered the translation of automated whole-spine 3D-3D registration with the planning CT, 3D navigation across all levels from a single image and intraoperative assessment of global spine alignment.

The limited longitudinal field-of-view of standard CBCT intraoperative imaging is due to the use of simple circular imaging trajectories and hardware design (detector length). One approach to extending the field-of-view is acquiring multiple circular acquisitions, each offset by a longitudinal table translation, and stitching together the individually reconstructed image volumes (10–12). Limitations to such an approach currently include the vendor-imposed restriction on the number of volumes that can be stitched together (typically 2), the requirement to manually translate the table between scans which extends scan time, and introduction of additional artifacts if the anatomy changes/moves between the scans, e.g. due to breathing, that are stitched together. An alternative approach is to use non-circular trajectories, such as a line-ellipse-line and reverse helical trajectory (13–15). To date, however, these trajectories have only been able to demonstrate incremental

increases in the longitudinal field-of view during phantom studies; 17 cm to 20 cm using the line-ellipse-line (13) and 17 cm to 27.4 cm using the reverse helical trajectory (15), respectively. Additionally, these trajectories have been realized solely by the gantry (rotation and translation) of fixed-room robotic CBCT imaging systems. This requires a gantry collision check over the entire extended field-of-view before imaging, increasing the potential for collision with equipment and personnel, especially in operating rooms where space is a premium.

Here, we implement a continuous multi-turn reverse helical imaging trajectory on a clinical fixed-room robotic CBCT system, combining real-time gantry rotation and patient table translation to extend the intraoperative field-of-view by a factor of 4 compared to standard CBCT. By delegating the longitudinal translation to the patient table, only the minimum amount of collision avoidance checks for the gantry rotation is required (i.e., that of a conventional circular acquisition). We believe that the extended intraoperative CBCT imaging field-of-view provided by the multi-turn reverse helical scan will find applications in a wide range of fields, both surgical and interventional. As a first demonstration of potential new clinical utility, we use the multi-turn reverse helical scan during a pedicle screw posterior fixation procedure on an ovine cadaver, providing accurate in-room assessment of pedicle screw insertion.

Materials and Methods

Multi-turn Reverse Helical Trajectory

A fixed-room robotic CBCT system (Siemens ARTIS pheno, Siemens Healthcare GmbH, Erlangen Germany) with additional real-time control over the C-arm and table movements was used to investigate the feasibility of extended longitudinal intraoperative imaging via a multi-turn reverse helical scan, Figure 1.

The multi-turn reverse helical scan consists of repeated continuous C-arm rotation, through a series of clockwise and anticlockwise rotations and simultaneous table translations. Initially, the table is positioned as close to the C-arm without triggering a collision warning or colliding with the subject. The C-arm begins at the maximum right anterior oblique angle, allowing full angular range (400° around the table) in every clockwise and anti-clockwise rotation. During each rotation, the C-arm rotates at constant speed (20°/s), currently limited by prototype control hardware (16, 17). Rotation speeds exceeding 45°/s are common in clinical use. In total, the C-arm completes 4×400° rotations (2 clockwise and 2 anticlockwise) and 1×200° clockwise rotation at the end of the scan, covering 1800°. To ensure data completeness at the extremes of the reconstructed image, the table remains stationary for the first 100° and last 200° of the C-arm rotations, minimizing the “overscan” region. During the remaining 1500° of C-arm rotation, the table is translated away from the C-arm at 10 mm/s, resulting in an effective pitch of 1. To allow continuous arc data to be collected without exerting high accelerations on the C-arm, the table is programmed to automatically reposition at the end of each C-arm rotation. The scan takes approximately 100 s to complete and x-ray projections are acquired continuously at 90 kV and 15 fps, resulting in a maximum of 1500 projections. Acquisition settings for the x-ray projections of 90 kV and 0.5 mAs were selected; however, the Automatic Exposure Control (AEC) could

not be turned off. As such, the kV and mAs were free to modulate in accordance with the in-built AEC parameters over the course of the multi-turn reverse helical scan. The kV and mAs for the multi-turn reverse helical scan were selected to match as closely as feasibly possible to the acquisition settings of the conventional CBCT scans used as a comparator (90 kV, 0.58 mAs) on the system. Additionally, although frame rates in excess of 30 fps for conventional 3D acquisitions are common in clinical use, due to the reduced gantry velocity increasing the scan time of the multi-turn reverse helical acquisition, 15 fps is preferable to limit the total number of projections acquired. If the gantry could rotate within the current clinically used velocities, the scan time could be reduced to approximately 30 seconds and then a frame rate of 30 fps would be used.

Prior to a multi-turn reverse helical scan, clearance and collision checks are completed to ensure anesthesia and monitoring tubes/wires are not being pulled during the table translation and that the gantry's rotation path is clear of equipment and personnel. To minimize the risk of tube/wire pulling during the table translation, these items were secured close to the table, preventing them from being dragged along the floor and into the path of the gantry. As the gantry remains stationary as it completes its rotation, only the minimum amount of clearance for the gantry rotation (i.e., that of a conventional circular acquisition) is required.

To determine if the table and C-arm trajectories of the proposed multi-turn reverse helical scan were reproducible, the system properties (position, velocity, and acceleration) of the table and C-arm were documented during 5 consecutive multi-turn reverse helical scans.

To examine the geometric accuracy of the 3D reconstructed image from the multi-turn reverse helical scan, a simple phantom constructed from plastic bricks was imaged. To quantify the accuracy of conducting length measurements on the multi-turn reverse helical images 42 plastic bricks, with 3 different sets of dimensions as shown in Figure 2 (A), were each individually measured on the 3D image from a multi-turn reverse helical scan and compared to the manufactured specifications. To quantify the accuracy of making angular measurements on the multi-turn reverse helical images an additional 4 plastic pieces were placed along the length of the phantom. Each piece contained 4 × 135°, 4 × 90° and 4 × 45° angles, as illustrated in Figure 2 (B).

To examine the image quality of the 3D reconstructed images from the multi-turn reverse helical scan, a Catphan 500 CT phantom was imaged. The Catphan 500 CT phantom contains 4 contrast cylinders (air, Teflon, low density polyethylene (LDPE) and acrylic) and 21 line pairs. The contrast-to-noise ratio of each of the contrast cylinders was compared between the multi-turn reverse helical and a conventional CBCT scan. The spatial resolution was examined via the line pair gauge, identifying when the gap within the line pairs was no longer able to be resolved in both the multi-turn reverse helical and a conventional CBCT scan.

Pedicle screw posterior fixation

As a first demonstration of potential new clinical utility, a pedicle screw posterior fixation procedure from the T1-T12, aided via 3D printed drill guides (18), was performed on an

ovine cadaver (AK, 4 years experience). The cadaver used in this study was provided by the Laboratory Animal Services at the University of Sydney, in accordance with the University's Animal Ethics Procedures. Ethics approval to sacrifice the animal had been obtained through the University's Animal Ethics Committee for previous, separate studies. The ovine cadaver was placed in the prone position. A midline posterior incision and approach was used. A subperiosteal dissection was performed on all the involved vertebrae. The areas where the 3D printed drill guides were to be positioned were cleaned of soft tissues. Stability of the drill guides was confirmed with gentle downward digital pressure. A 4.2 mm drill was used to create a pilot hole. A ball-tipped pedicle probe was used to confirm no palpable breach. The templated Evolution Surgical (Sydney, Australia) pedicle screw was then inserted.

A "gold-standard" pre-operative conventional CT scan (GE Revolution Evo, GE Healthcare, United States of America), along with a series of conventional CBCT scans and a multi-turn reverse helical scans (Siemens ARTIS pheno, Siemens Healthcare GmbH, Germany) were acquired before and after screw placement. The individual conventional CBCT scans took 5 seconds each to acquire (17 cm field-of-view, 397 projections/scan at 90 kV), with manual table translations between each scan to capture the cervical and thoracic spine of approximately 30–60 seconds per translation. After the procedure, the individual scans (both pre-operative and post-operative) were manually aligned and stitched together using MATLAB (MathWorks, United States of America) to form the final volumes. Stitching of more than 2 conventional CBCT scans using the inbuilt software of the fixed-room robotic CBCT system used is currently not possible.

The accuracy of the screw insertion was evaluated with post-operative images from the conventional CT, stitched conventional CBCT and the multi-turn reverse helical scans using the Gertzbein-Robbins grading system and via calculating the mean axial and sagittal screw error, measured using an onscreen protractor (18, 19) from 2 expert observers. For all measurements, the intraclass correlation coefficient (ICC) (20) was calculated to determine observer reliability.

Geometry calibration, image reconstruction and metal artifact reduction

Due to the custom trajectory and inaccuracies in the positional recording from the system, a 3D-2D registration was performed to calibrate the geometry of each projection (21) to enable high-resolution reconstructions. To facilitate this process, the conventional CBCT scans were stitched together and used as the registration target. Forward projections from the target using the machine-recorded geometry were generated to initialize the registration. Then, the true geometry was found iteratively by maximizing the similarity between the forward projections and the measurements, using gradient orientation as the similarity metric (22). A model-based iterative reconstruction algorithm was applied to accommodate the custom multi-turn reverse helical trajectory, using a Penalized Weighted Least Squares objective (23) and quadratic penalty. For the geometric accuracy scans, 20 iterations with 113 ordered subsets were run with 0.25 mm^3 isotropic voxels, taking 1 hour to complete (178 seconds/iteration). For the image quality scan of the Catphan 500 CT phantom, 100 iterations with 2 ordered subsets were run with 0.4737 mm^3 isotropic voxels, taking 22 minutes to complete. For both pre- and post-operative acquisitions during the pedicle

screw posterior fixation procedure, 200 iterations and 15 ordered subsets were run for each reconstruction with 0.5 mm^3 isotropic voxels, taking 20 hours to complete (~6 minutes/iteration). A simple metal artifact reduction algorithm (24) was implemented to reduce the metal artifacts caused by the pedicel screws in the post-operative multi-turn reverse helical scan. The metal artifact reduction involves 1) creating an initial reconstruction and segmenting out the metal volume, 2) creating a metal-free reconstruction by replacing metal pixels by interpolation, and 3) adding in the metal volume. Regions outside the field-of-view of the detector were truncated in the reconstructions.

Reconstructed Image Quality – Ovine Cadaver

The 3D reconstructed image quality of the pre- and post-operative multi-turn reverse helical and stitched conventional CBCT scans of the ovine cadaver were compared via the metrics of Contrast-to-Noise Ratio, Tissue Interface Width and Structural Similarity Index Metric. The Contrast-to-Noise Ratio was calculated as the absolute difference between average voxel values in the bone and surrounding soft tissue, divided by the standard deviation in voxel values (25). Structural similarity between the multi-turn reverse helical and conventional CBCT volumes was computed using the MATLAB (MathWorks, United States of America) function, Structural Similarity Index Metric, with default values (26). The Tissue Interface Width was derived from Tissue Interface Sharpness (27), computed by first placing a 5×5×40 voxel region-of-interest at a tissue interface, in this case bone. Sigmoid functions were then fitted to 25 line profiles, where the Tissue Interface Sharpness was taken as the average sigmoid gradient. Tissue Interface Sharpness was converted to Tissue Interface Width as the distance in millimeters over which the average sigmoid changed from 10% to 90% intensity.

Results

System properties, geometric accuracy, and image quality

The system-recorded properties (position, velocity, and acceleration) of the table and C-arm recorded during 5 consecutive multi-turn reverse helical scans are provided in Figure 3. Across the series of 5 scans, a total scan range of 1805.6 ± 3.4°, total table translation of 642.3 ± 0.4 mm and scan time of 101.2 ± 0.4 s was observed. However, at the 60 s mark of each scan, the C-arm consistently paused momentarily before resuming its programmed rotation. The pause has been observed in every implementation of the trajectory to date but does not have any observable effect on image quality. No pause in the table translation has been observed.

Examples of the 3D reconstructed images from imaging the geometric accuracy phantom (Figure 2) with the multi-turn reverse helical scan are provided in Figure 4. The average difference in the measured to actual dimensions of the length of the middle row within each of the 5 main brick structures, Figure 4(A), was 0.3 ± 0.2 mm ($n = 20$). The average difference in the measured to actual dimensions (length, width, and height) of the 42 individual plastic bricks, Figure 4(B) was 0.2 ± 0.1 mm ($n = 126$). The average difference in the measured to actual angles of the 4 additional pieces, Figure 4(C) was 0.2 ± 0.1° ($n = 48$).

Examples of the 3D reconstructed images from imaging the Catphan 500 CT phantom with a conventional CBCT and the multi-turn reverse helical scan are provided in Figure 5. Considering the contrast cylinders first, the acrylic cylinder could not be resolved in either the conventional CBCT or multi-turn reverse helical scan. As such, the contrast-to-noise ratio was only calculated over the air (3.00 conventional CBCT, 2.94 multi-turn reverse helical), Teflon (3.00 conventional CBCT, 2.90 multi-turn reverse helical), and LDPE (2.62 conventional CBCT, 1.81 multi-turn reverse helical) cylinders respectively. In terms of spatial resolution, the conventional CBCT scan was able to resolve the 8^{th} line pair (gap size 0.063 cm), while the multi-turn reverse helical scan was able to resolve the 7^{th} line pair (gap size 0.071 cm).

Ovine cadaver

The pre-operative reconstructed 3D images of the ovine cadaver using conventional CT, the multi-turn reverse helical scan and a series of conventional stitched CBCT scans are shown in Figure 6 (coronal view). Gaps in the stitched CBCT images are attributable to manual error in table positioning. The pre-operative multi-turn reverse helical scan acquired a total of 1388 projections, compared to a total of 1985 projections from the stitched CBCT scans (5 scans). The post-operative reconstructed 3D images of the ovine cadaver using conventional CT, the multi-turn reverse helical scan and a series of conventional CBCT scans stitched together (6 individual scans) are shown in Figure 7 (coronal and sagittal views). The post-operative multi-turn reverse helical scan acquired a total of 1350 projections, compared to a total of 2382 projections from the stitched CBCT scans (6 scans). Pre- and post-operative imaging with the multi-turn reverse helical scan provided axial coverage of 80 cm, enabling clear visualization of the skull and vertebral endplates from C1 through to T11. At the right-hand edge of both the pre- and post-operative reconstructed 3D images from the multi-turn reverse helical scan, there is evidence that the beginning of the target volume has been undersampled during the acquisition. Specifically, the first 2 cm of both volumes display visual artifacts, partially obscuring the underlying anatomy compared to the stitched conventional CBCT scans within that region. These artifacts are due to the gantry only passing through 100° prior to the table translation commencing, and therefore failing to capture complete data of the anatomy of interest before it moves out of the detector field-of-view. These artifacts did not impact the vertebral assessment pre- or post-operatively.

In total, 24 screws were inserted in 12 thoracic vertebrae. The post-operative multi-turn reverse helical scan identified 4 cortical breaches (1 grade B (T7L), 2 grade C (T6L and T9R) and 1 grade E (T1L)), that were confirmed with the post-operative CT and CBCT scans. Post-operative axial views of the T6 vertebra using conventional CT, the multi-turn reverse helical scan and a series of conventional CBCT scans stitched together are shown in Figure 8. An additional perforation at the T12R vertebra was observed in the post-operative CT scan. Due to the size and position of the sheep on the operating table, the T12 vertebra was outside the field-of-view for both the multi-turn reverse helical and conventional CBCT scans. The cortical breaches were due to either a small/unstable guide (T1L) or misplaced guide (T6L, T7L, and T9R). During the procedure, the T7 guide was mistakenly placed on

the T6 vertebra, and pedicle screws inserted. The mistake was only identified at T10, leading to incorrect screw placement between T6-T9 inclusive.

Directly comparing the measured axial and sagittal screw angle of all 22 screws (T1-T11) visible in the post-operative multi-turn reverse helical and conventional CT scans revealed an average difference of 3.3 ± 2.6° in axial angle and 1.9 ± 1.5° in the sagittal angle, as measured by two expert observers. Comparing the measured axial and sagittal screw angle visible within the multi-turn reverse helical and the stitched conventional CBCT scans, an average difference of 3.2 ± 2.7° in axial angle and 2.6 ± 2.2° in the sagittal angle was observed. The ICC for the axial angle measurements between the two expert observers was 0.993 (conventional CT), 0.957 (multi-turn reverse helical) and 0.976 (stitched conventional CBCT scans), indicating excellent reliability (20). Similarly for the sagittal screw angle measurements, the ICC between the two expert observers was 0.900 (conventional CT), 0.984 (multi-turn reverse helical) and 0.9811 (stitched conventional CBCT scans), again indicating excellent reliability (20).

To avoid influence of metal artifacts, the image quality metrics of Contrast-to-Noise Ratio and Tissue Interface Width were computed over the C3 vertebrae and nearby soft tissue in both the pre- and post-operative images. The Contrast-to-Noise Ratio of the multi-turn reverse helical scan measured on the pre- and post-operative images was 1.90 and 1.85 respectively, compared to 1.93 and 1.88 from the stitched conventional CBCT scans. Similarly, the Tissue Interface Width of the multi-turn reverse helical scan measured on the pre- and post-operative images was 3.28 mm and 2.31 mm respectively, compared to 3.10 mm and 3.36 mm from the stitched conventional CBCT scans. The Structural Similarity Index Metric between the multi-turn reverse helical and stitched conventional CBCT was calculated on the pre-operative scans only to again avoid the influence of metal artifacts. The Structural Similarity Index Metric over the C3 vertebra was 0.828 and the T8 vertebra was 0.949.

Discussion

This study demonstrates the feasibility of implementing a multi-turn reverse helical scan in real-time on a robotic CBCT system, extending the length of the intraoperative 3D field-of-view to 80 cm. The geometric accuracy of the multi-turn reverse helical scan matched that of a conventional CBCT scan, evidenced by no observable distortion in dimensional or angular measurements made throughout the volume when imaging a simple geometric phantom. Additionally, when imaging a Catphan 500 phantom, the multi-turn reverse helical scan provided comparable contrast-to-noise ratio measurements for the air and Teflon contrast cylinders, compared with the conventional CBCT scan. However, the LDPE contrast cylinder was more difficult to resolve for the multi-turn reverse helical, resulting in a lower contrast-to-nose ratio compared to the conventional CBCT scan. The spatial resolution, as determined by the line pair gauge in the Catphan 500 phantom, was slightly higher for the multi-turn reverse helical scan compared to the conventional CBCT scan, but still enabled sub millimeter resolution. The potential clinical utility of the multi-turn reverse helical scan was also investigated in an ovine cadaver in a posterior pedicle screw fixation procedure. Specifically, the multi-turn reverse helical scan matched the image

quality of current conventional intraoperative CBCT (through metrics of Contrast-to-Noise Ratio, Tissue Interface Width and Structural Similarity Index Metric) and provided post-operative assessment (pedicle screw exposure/perforation and pedicle screw angle analysis) matching that of conventional CT. These results are consistent with other recent studies in the literature comparing conventional intraoperative CBCT imaging with CT imaging during orthopedic interventions (28, 29).

While stitching together a series of conventional CBCT scans was able to provide the same axial coverage as the multi-turn reverse helical, there are many limitations to this approach. Manual alignment and stitching of the individual volumes need to be completed off-line away from the operating room, resulting in significant stitching artifacts and additional processing time. Additional artifacts can also be introduced if the anatomy changes/moves between consecutive scans, e.g., due to breathing, that are being stitched together. Finally, the series of conventional CBCT scans also leads to a larger number of total projections being acquired compared to the multi-turn reverse helical scans.

The results of the pedicle screw fixation procedure in the ovine cadaver highlight the potential for the multi-turn reverse helical to assess cortical breaches and evaluate pedicle screw angle insertion. Having this information available within the operating room will provide surgeons with the ability to immediately identify and address deviations from the surgical plan, reducing the need for additional correction procedures (28).

The focus in this study was on imaging the spine; however, extended longitudinal capability could also find utility in interventional radiology, allowing the entire aorta or long vascular “runoff” exams (30), and interventional neurology, allowing complete stroke assessment from the head to the top of the aorta branch (31), to be captured in a single image, for example. Here, we demonstrated the ability of the multi-turn reverse helical scan to provide 80 cm of longitudinal 3D field-of-view coverage, however, any field-of-view range between 17–80 cm is possible by simply reducing the number of turns in the reverse helix. To ensure data completeness at the extremes of the reconstructed images, future implementations of the multi-turn reverse helical scan will ensure the gantry rotates through 200° (current implementation only 100°) prior to the table translation commencing, eliminating the possibility of image artifacts from under sampled regions. To extended beyond 80 cm, the gantry can be positioned laterally to the table, allowing an increased number of turns in the reverse helix. Then, the maximum extension is only limited only by hardware constraints (i.e., collision between table and stand). Looking to future systems, the intraoperative CBCT field-of-view could also be extended further with the addition of wider detectors and increased C-arm gantry reach.

There are a number of limitations associated with the current experimental implementation of the multi-turn reverse helical scan presented here. First, the velocity limits on the C-arm rotation (20°/s) and table translation (90 mm/s) imposed when operating the system with the additional real-time control hardware. Not only do these limits increase the scan time (currently 100 s), but they also reduce the possibility of optimizing the helical pitch and exploring ways to further reduce the total number of projections required. Second, the CBCT system used in this study was not designed to allow 3D image reconstruction from

arbitrary trajectory scans. Therefore, to enable 3D image reconstruction of the multi-turn reverse helical scans, projections images were acquired using in-built protocols optimized for 2D viewing. The in-built 2D imaging protocols have no restrictions on the imaging trajectory during image acquisition aside from the hardware constraints of the system. However, the in-built 2D imaging protocols do not allow for direct kV and mAs matching with the conventional CBCT scans due to not being able to turn off the AEC. The acquisition settings of the multi-turn reverse helical scan were selected to match as closely as feasibly possible to the conventional scans at the start of the scan, but the kV and mAs were free to modulate in accordance with the in-built AEC parameters over the course of the scan. As a result, presently a direct dose comparison between the multiple conventional CBCT scans stitched together and the multi-turn reverse helical scan is not possible. However, total projection number can act as a surrogate measure, indicating the potential to reduce imaging dose by using the multi-turn reverse helical scan compared with multiple conventional CBCT scans stitched together for the same intraoperative 3D coverage. Third, the reconstruction times of the multi-turn reverse helical are currently prohibitive for the scan to be implemented clinically. The long scan time is due to the large volume of the scan, total number of projections acquired, and the iterative nature of the reconstruction method used. Fourth, geometric calibration is currently required (completed using 3D-2D registration algorithms) in post-processing for high-resolution reconstructions of diagnostic quality, due to inaccuracies in the system-recorded geometry data.

The multi-turn reverse helical scan outlined here is potentially applicable to all fixed-room robotic CBCT systems, regardless of vendor. Currently, however, no clinically available robotic imaging system enables user access to the control system necessary to perform this study. Vendor support will overcome the limitations outlined above and enable the multi-turn reverse helical scan to be clinically translated. For example, with vendor support, the rotation velocity (commonly exceeding 45°/s in clinical use) and table translation velocity could be increased, significantly reducing scan times and providing scope to optimize the pitch for each patient. Vendor support would also allow the projection acquisition to occur with settings of kV and mAs that are optimized for 3D image reconstruction. The multi-turn reverse helical scan, with vendor support, could also be commissioned and calibrated in the same way as current conventional 3D protocols on the system. This would eliminate the current reliance on system-recorded geometry data or need for prior scans to facilitate 3D-2D registration for accurate geometric calibration.

A final limitation of the current study was the use of a cadaver, reducing the additional imaging complexities faced during interventional procedures, such as blurring due to physiological movement of the patient (i.e., breathing lungs and beating heart). Future studies will look to quantify this effect and examine the possibility of integrating adaptive imaging strategies to mitigate physiological motion (16, 17). Additionally, during future iterations of the multi-turn reverse helical scan where the gantry velocity can match that of current clinical 3D imaging (velocities > 45°/s, reducing the scan time to approximately 30 s), the possibility of acquiring images during breath hold to mitigate motion blur needs to be investigated.

This is the first report of a continuous multi-turn reverse helical CBCT scan to image an animal specimen within the context of an interventional procedure. This study represents a key step in clinical translation of multi-turn reverse helical scanning to extend the longitudinal field of view, visualize long surgical constructs, and also provide intraoperative verification of device placement.

Acknowledgments

Funding Information:

This research was supported in part by National Institute of Health grant R01EB02717, Cancer Institute of New South Wales Fellowship 2021/ECF1293, and by Research Agreement (G201166 IPA2) with Siemens Healthineers.

References:

1. Verma SK, Singh PK, Agrawal D, et al. O-arm with navigation versus C-arm: a review of screw placement over 3 years at a major trauma center. British Journal of Neurosurgery. 2016;30(6):658–61. [PubMed: 27454157]
2. Summers LE, Kouri JG, Yang M, Patrick Jacob R. Odontoid Screw Placement Using Isocentric 3-dimensional C-arm Fluoroscopy. Clinical Spine Surgery. 2008;21(1).
3. Khanna AR, Yanamadala V, Coumans J-V. Effect of intraoperative navigation on operative time in 1-level lumbar fusion surgery. Journal of Clinical Neuroscience. 2016;32:72–6. [PubMed: 27364319]
4. Kim TT, Drazin D, Shweikeh F, et al. Clinical and radiographic outcomes of minimally invasive percutaneous pedicle screw placement with intraoperative CT (O-arm) image guidance navigation. Neurosurgical Focus FOC. 2014;36(3):E1.
5. Scarone P, Vincenzo G, Distefano D, et al. Use of the Airo mobile intraoperative CT system versus the O-arm for transpedicular screw fixation in the thoracic and lumbar spine: a retrospective cohort study of 263 patients. Journal of Neurosurgery: Spine SPI. 2018;29(4):397–406.
6. Siewerdsen JH, Moseley DJ, Burch S, et al. Volume CT with a flat-panel detector on a mobile, isocentric C-arm: Pre-clinical investigation in guidance of minimally invasive surgery. Medical Physics. 2005;32(1):241–54. [PubMed: 15719975]
7. Richter PH, Yarboro S, Kraus M, Gebhard F. One year orthopaedic trauma experience using an advanced interdisciplinary hybrid operating room. Injury. 2015;46:S129–S34. [PubMed: 26542859]
8. Wang L, Traub J, Heining SM, et al. Long Bone X-Ray Image Stitching Using Camera Augmented Mobile C-Arm. In: Metaxas D, Axel L, Fichtinger G, Székely G, eds. Medical Image Computing and Computer-Assisted Intervention – MICCAI 2008, 2008// 2008. Berlin, Heidelberg. Springer Berlin Heidelberg: 578–86.
9. Zhang X, Uneri A, Wu P, et al. Long-length tomosynthesis and 3D-2D registration for intraoperative assessment of spine instrumentation. Physics in Medicine & Biology. 2021;66(5):055008. [PubMed: 33477120]
10. Köhler T, Proksa R, Grass M. A fast and efficient method for sequential cone-beam tomography. Medical Physics. 2001;28(11):2318–27. [PubMed: 11764039]
11. Rafic KM, Timothy Peace SB, Manu M, et al. A rationale for cone beam CT with extended longitudinal field-of-view in image guided adaptive radiotherapy. Physica Medica. 2019;62:129–39. [PubMed: 31153392]
12. Zheng D, Lu J, Jefferson A, et al. A protocol to extend the longitudinal coverage of on-board cone-beam CT. Journal of Applied Clinical Medical Physics. 2012;13(4):141–51.
13. Guo Z, Lauritsch G, Maier A, et al. C-arm CT imaging with the extended line-ellipse-line trajectory: first implementation on a state-of-the-art robotic angiography system. Physics in Medicine & Biology. 2020;65(18):185016. [PubMed: 32512552]
14. Tan J, Li HH, Klein E, et al. Physical phantom studies of helical cone-beam CT with exact reconstruction. Medical Physics. 2012;39(8):4695–704. [PubMed: 22894394]

15. Yu Z, Maier A, Lauritsch G, et al. Axially Extended-Volume C-Arm CT Using a Reverse Helical Trajectory in the Interventional Room. IEEE Transactions on Medical Imaging. 2015;34(1):203–15. [PubMed: 25167545]
16. Reynolds T, Dillon O, Prinable J, et al. Toward improved 3D carotid artery imaging with Adaptive CaRdiac cOne BEAm computed Tomography (ACROBEAT). Medical Physics. 2020;47(11):5749–60. [PubMed: 32969492]
17. Reynolds T, Dillon O, Prinable J, et al. Adaptive CaRdiac cOne BEAm computed Tomography (ACROBEAT): Developing the next generation of cardiac cone beam CT imaging. Medical Physics. 2021;48(5):2543–52. [PubMed: 33651409]
18. Kanawati A, Rodrigues Fernandes RJ, Gee A, et al. The Development of Novel 2-in-1 Patient-Specific, 3D-Printed Laminectomy Guides with Integrated Pedicle Screw Drill Guides. World Neurosurgery. 2021;149:e821–e7. [PubMed: 33540103]
19. Mathew JE, Mok K, Goulet B. Pedicle violation and Navigational errors in pedicle screw insertion using the intraoperative O-arm: A preliminary report. International journal of spine surgery. 2013;7:e88–e94. [PubMed: 25694911]
20. Koo TK, Li MY. A Guideline of Selecting and Reporting Intraclass Correlation Coefficients for Reliability Research. Journal of chiropractic medicine. 2016;15(2):155–63. [PubMed: 27330520]
21. Ouadah S, Stayman JW, Gang GJ, et al. Self-calibration of cone-beam CT geometry using 3D-2D image registration. Physics in medicine and biology. 2016;61(7):2613–32. [PubMed: 26961687]
22. De Silva T, Uneri A, Ketcha MD, et al. 3D–2D image registration for target localization in spine surgery: investigation of similarity metrics providing robustness to content mismatch. Physics in Medicine and Biology. 2016;61(8):3009–25. [PubMed: 26992245]
23. Fessler JA. Penalized weighted least-squares image reconstruction for positron emission tomography. IEEE Transactions on Medical Imaging. 1994;13(2):290–300. [PubMed: 18218505]
24. Kalender WA, Hebel R, Ebersberger J. Reduction of CT artifacts caused by metallic implants. Radiology. 1987;164(2):576–7. [PubMed: 3602406]
25. Shieh C-C, Kipritidis J, O'Brien RT, et al. Image quality in thoracic 4D cone-beam CT: A sensitivity analysis of respiratory signal, binning method, reconstruction algorithm, and projection angular spacing. Medical Physics. 2014;41(4):041912. [PubMed: 24694143]
26. Dillon O, Keall PJ, Shieh C-C, O'Brien RT. Evaluating reconstruction algorithms for respiratory motion guided acquisition. Physics in Medicine & Biology. 2020;65(17):175009. [PubMed: 32485686]
27. Riblett MJ, Christensen GE, Weiss E, Hugo GD. Data-driven respiratory motion compensation for four-dimensional cone-beam computed tomography (4D-CBCT) using groupwise deformable registration. Medical Physics. 2018;45(10):4471–82. [PubMed: 30118177]
28. Burström G, Cewe P, Charalampidis A, et al. Intraoperative cone beam computed tomography is as reliable as conventional computed tomography for identification of pedicle screw breach in thoracolumbar spine surgery. European Radiology. 2021;31(4):2349–56. [PubMed: 33006659]
29. Nevzati E, Fandino J, Schatlo B, et al. Validation and accuracy of intraoperative CT scan using the Philips AlluraXper FD20 angiography suite for assessment of spinal instrumentation. British Journal of Neurosurgery. 2017;31(6):741–6. [PubMed: 28282990]
30. Preuß A, Schaafs L-A, Werncke T, et al. Run-Off Computed Tomography Angiography (CTA) for Discriminating the Underlying Causes of Intermittent Claudication. PloS one. 2016;11(4):e0152780–e. [PubMed: 27054846]
31. Furtado AD, Adraktas DD, Brasic N, et al. The Triple Rule-Out for Acute Ischemic Stroke: Imaging the Brain, Carotid Arteries, Aorta, and Heart. American Journal of Neuroradiology. 2010;31(7):1290. [PubMed: 20360341]

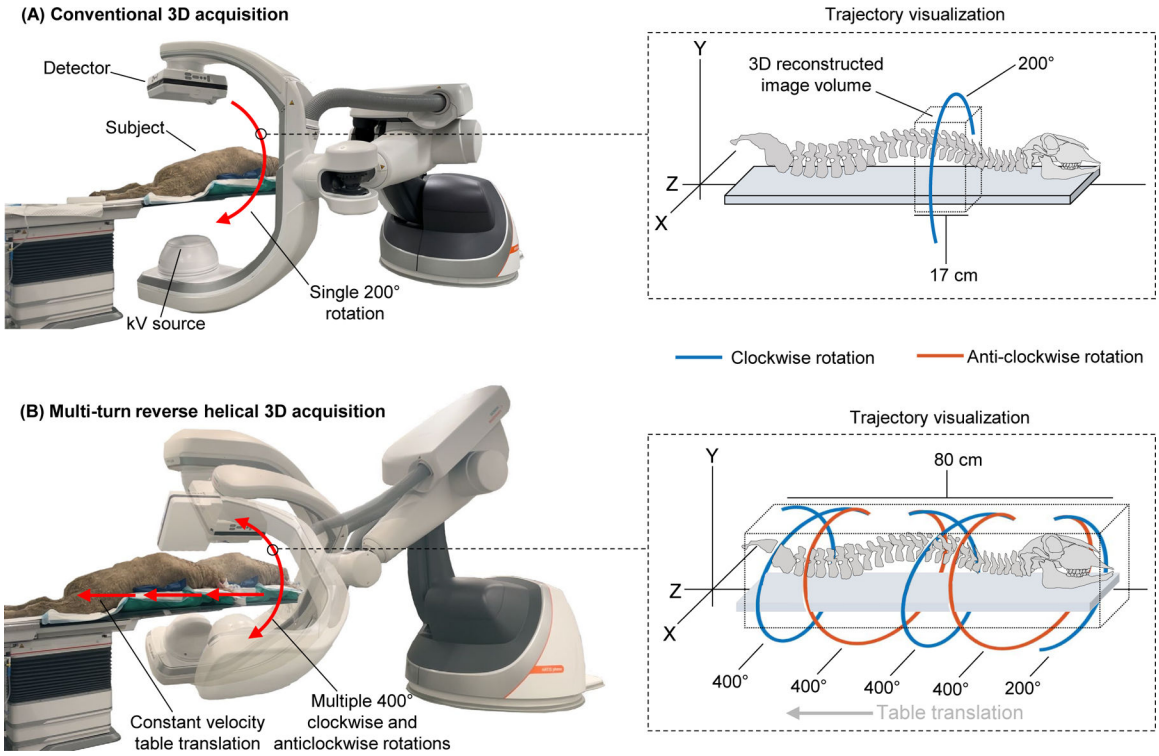

Figure 1.

Visualization of the imaging trajectory and longitudinal coverage during intraoperative CBCT imaging for a spinal pedicle screw posterior fixation procedure with a fixed-room robotic imager using (A) conventional circular acquisition (17 cm axial coverage) and (B) a multi-turn reverse helical acquisition (80 cm axial coverage).

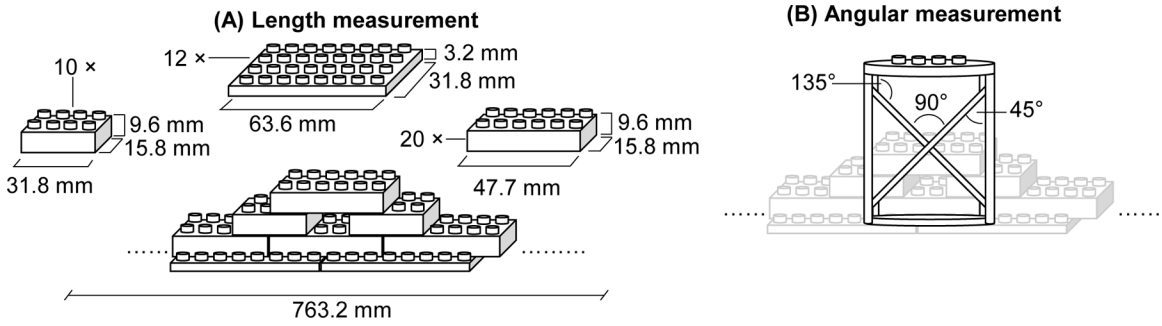

Figure 2.

Schematics of the phantom (constructed from 4 types of plastic bricks with specific dimensions and angular properties) used during the geometric accuracy assessment of the multi-turn reverse helical scan for (A) length and (B) angular measurements.

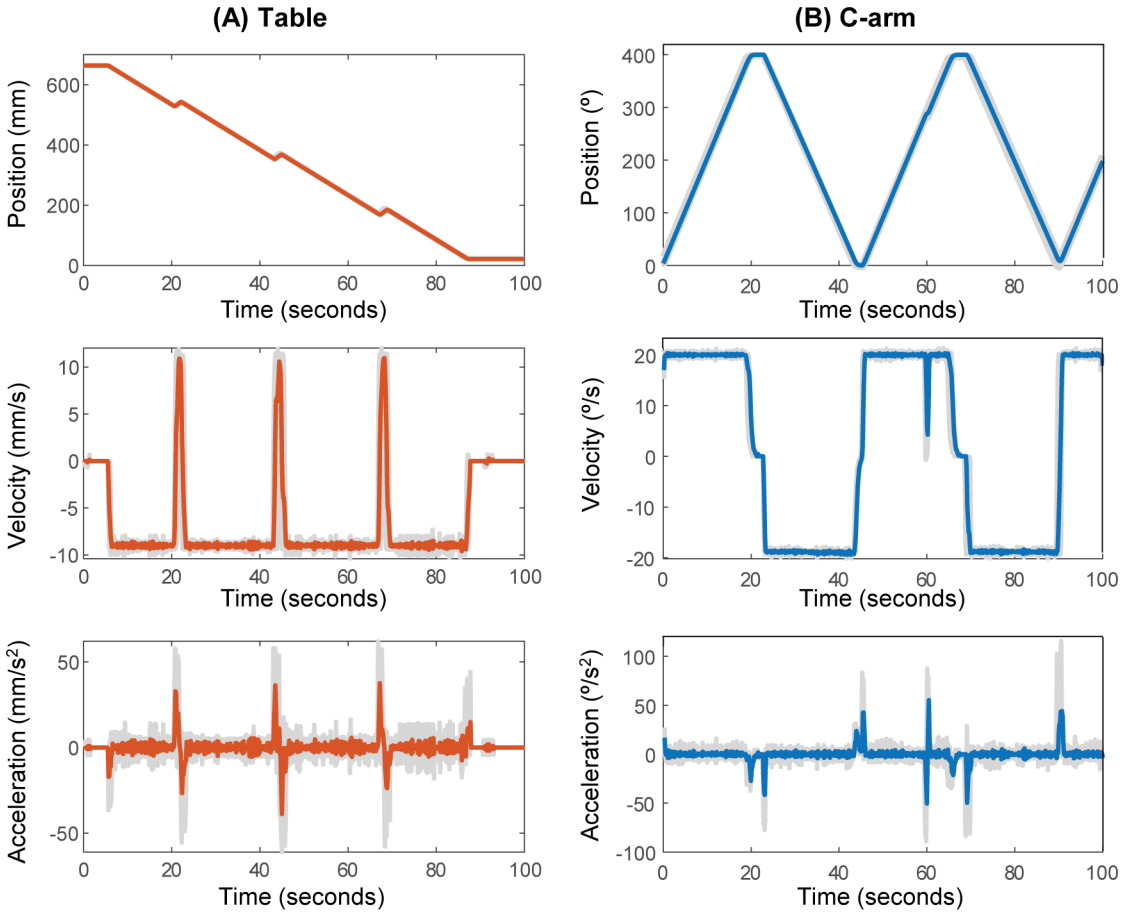

Figure 3.

System recorded motion properties (position, velocity and acceleration) of the (A) table and (B) C-arm during 5 consecutive multi-turn reverse helical scans on a fixed-room robotic CBCT system with additional real-time control. Colored lines display the average of five scans, while the light grey lines are the individual scans.

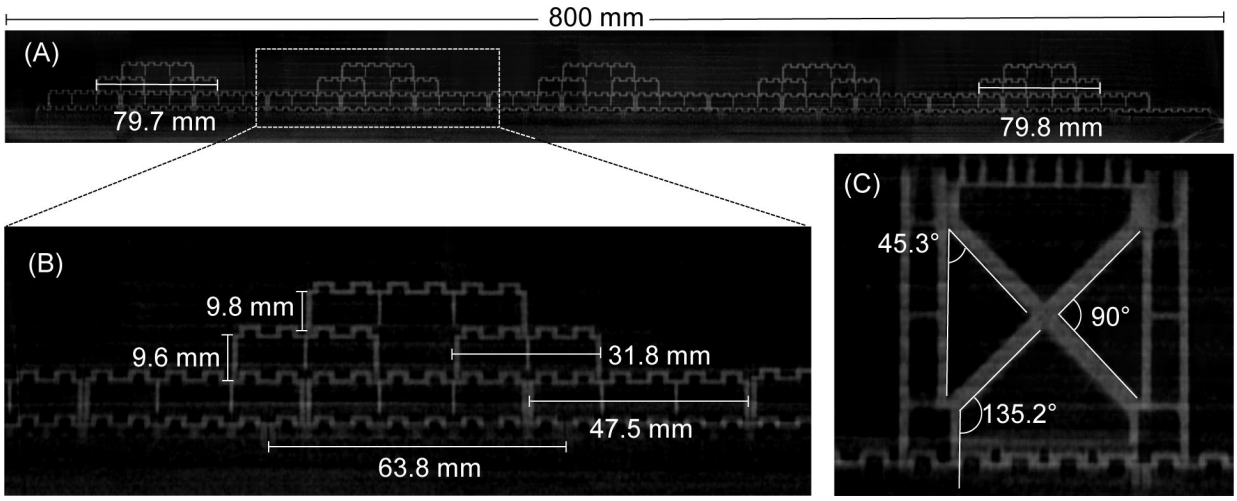

Figure 4.

Examples of the reconstructed 3D images of the geometric accuracy phantom from the multi-turn reverse helical scan, including on-screen measurements. Intensity window display [0.08, 0.04] mm^{-1}.

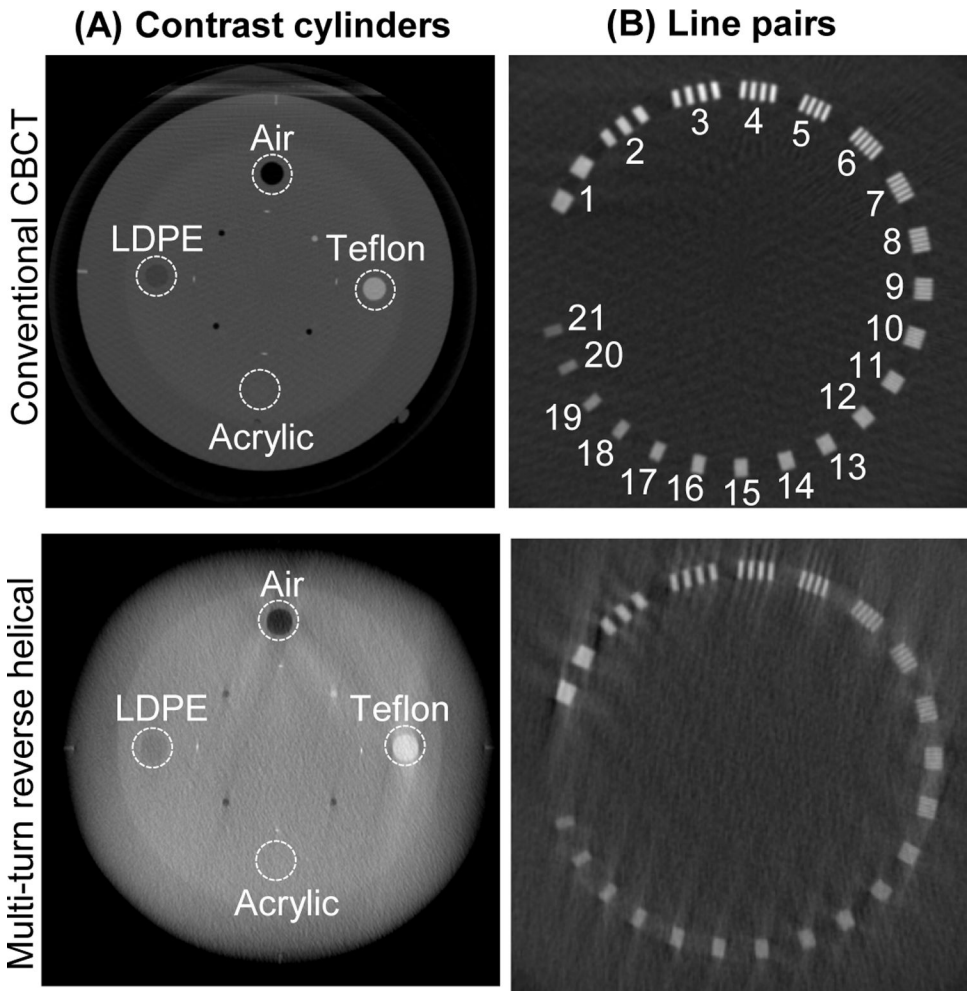

Figure 5.

Axial slices from the reconstructed 3D images of the Catphan 500 phantom from a conventional CBCT scan and the multi-turn reverse helical scan showing the (A) the 4 contrast cylinders and (B) 21 line pairs. Intensity window display [0.021, 0.027] mm^{-1}.

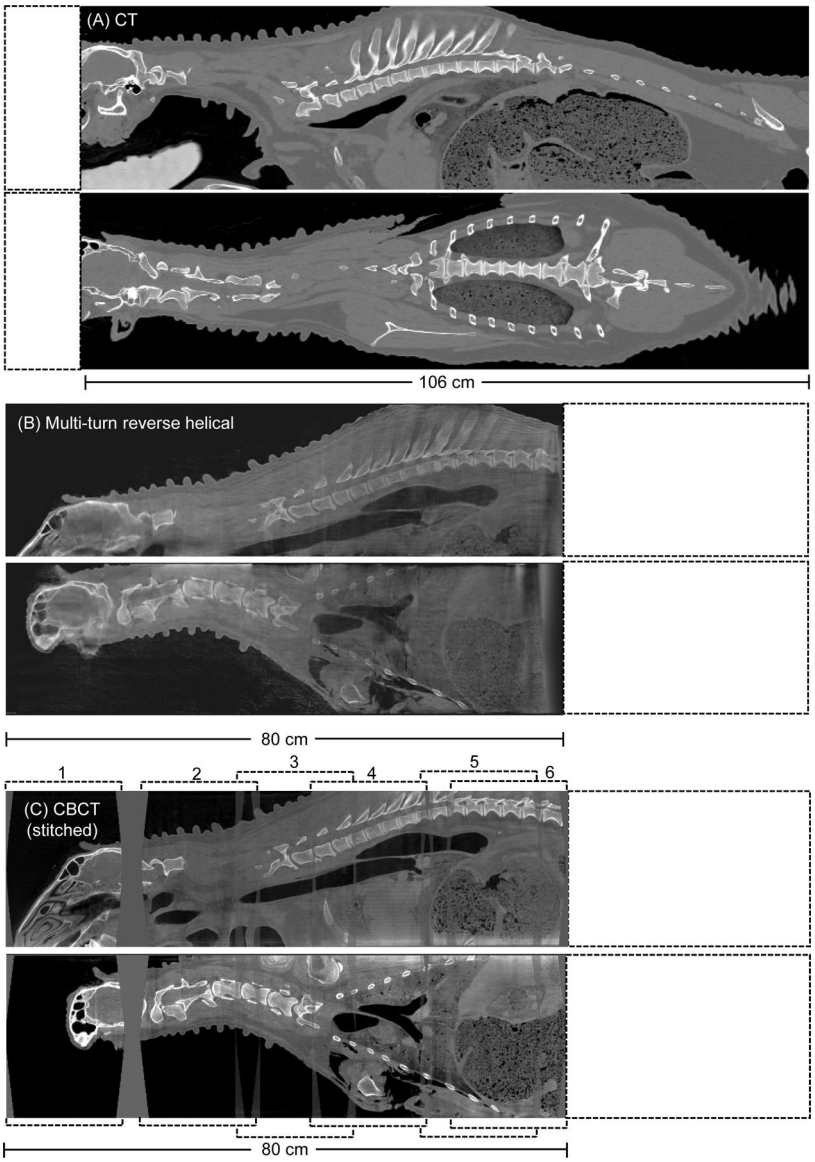

Figure 6.

Pre-operative reconstructed 3D images (sagittal and coronal view) of an ovine cadaver acquired from (A) conventional CT, (B) the multi-turn reverse helical and (C), a series of conventional CBCT scans stitched together (numbered 1 through 6). Intensity window display for the conventional CT scan [2000, 100] HU. Intensity window display for the multi-turn reverse helical and stitched conventional CBCT scans [0.063, 0.025] mm^{-1}.

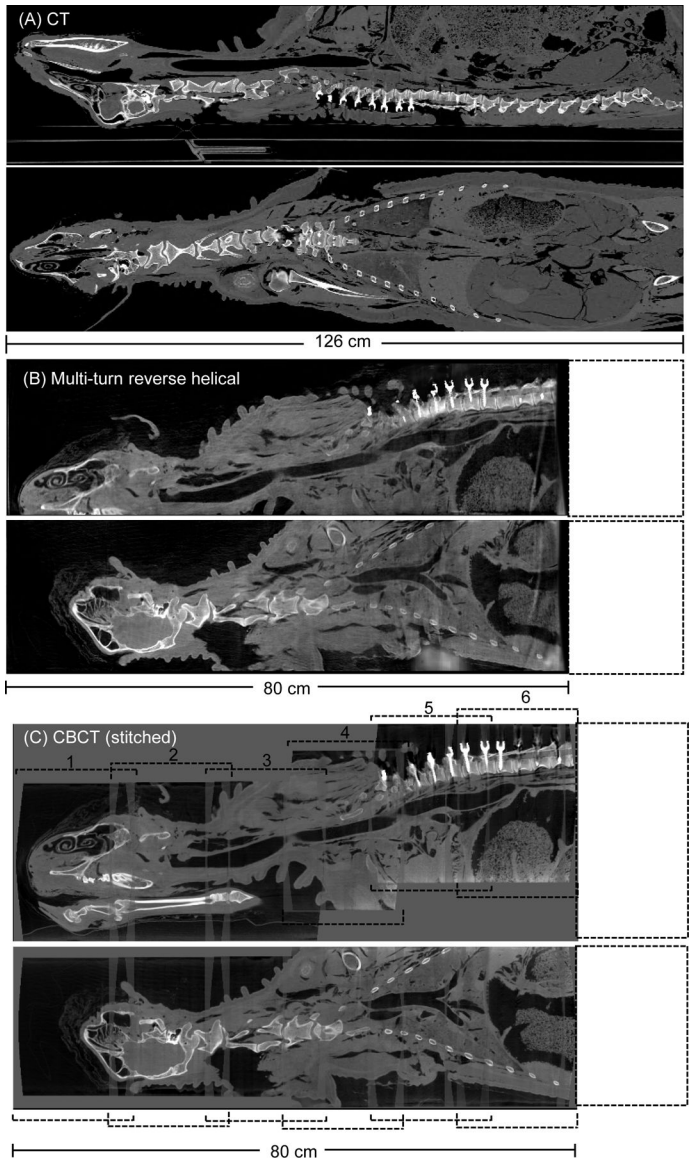

Figure 7.

Post-operative reconstructed 3D images (sagittal and coronal view) of an ovine cadaver following a pedicle screw posterior fixation from T1-T12 acquired from (A) conventional CT, (B) the multi-turn reverse helical and (C), a series of conventional CBCT scans stitched together (numbered 1 through 6). All images reconstructed with metal artifact reduction (MAR) algorithms (in-built MAR for the conventional CT and CBCT). Intensity window display for the conventional CT scan [640, 800] HU. Intensity window display for the multi-turn reverse helical and stitched conventional CBCT scans [0.063, 0.025] mm^{-1}.

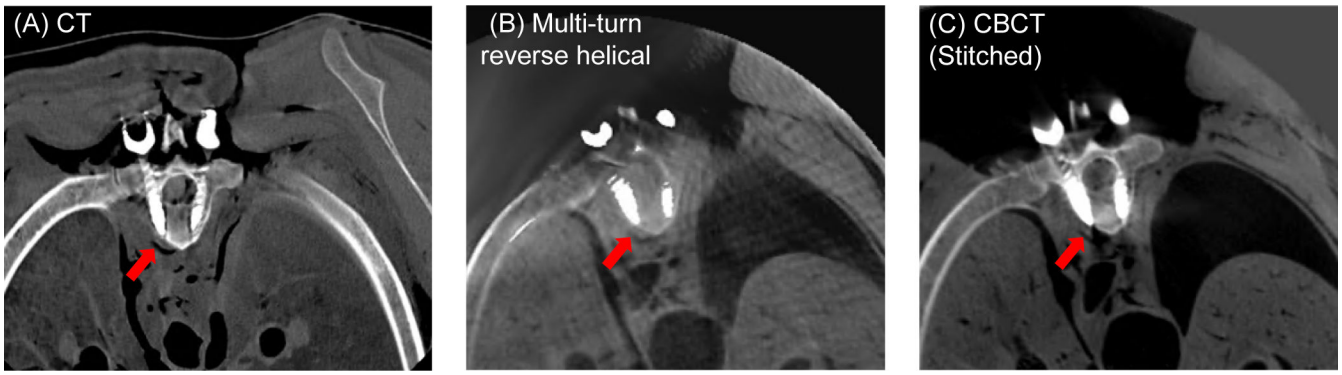

Figure 8.

The reconstructed 3D images (axial view) of the T6 vertebra of an ovine cadaver following the pedicle screw insertion using (A) conventional CT (B) the multi-turn reverse helical scan and (C) a series of conventional CBCT scans stitched together. All images reconstructed with metal artifact reduction (MAR) algorithms (in-built MAR for the conventional CT and CBCT). Intensity window display for the conventional CT scan [640, 800] mm^{-1}. Intensity window display for the multi-turn reverse helical and stitched conventional CBCT scans [0.063, 0.025] mm^{-1}.